Research Article Vol. 5, No. 12 / December 2018 / Optica 1557

Suppression of near-field coupling in plasmonic antennas on epsilon-near-zero substrates

Clayton T. DeVault,[1,4,†,*] Vladimir A. Zenin,[2,†] Anders Pors,[2] Krishnakali Chaudhuri,[3,4] Jongbum Kim,[3,4] Alexandra Boltasseva,[3,4] Vladimir M. Shalaev,[3,4] and Sergey I. Bozhevolnyi[2]

[1]Department of Physics and Astronomy, Purdue University, West Lafayette, Indiana 47907, USA
[2]SDU Nano Optics, University of Southern Denmark, Campusvej 55, DK-5230 Odense M, Denmark
[3]School of Electrical and Computer Engineering, Purdue University, West Lafayette, Indiana 47907, USA
[4]Birck Nanotechnology Center, Purdue University, West Lafayette, Indiana 47907, USA
*Corresponding author: cdevault@purdue.edu

Received 4 June 2018; revised 8 October 2018; accepted 12 November 2018 (Doc. ID 334252); published 4 December 2018

Epsilon-near-zero (ENZ) media are an emerging class of nanophotonic materials that engender electromagnetic fields with small phase variation due to their approximately zero permittivity. These quasi-static fields facilitate several unique optical properties, such as subwavelength confinement, arbitrary wavefront control, and enhanced light–matter interactions, which make ENZ materials promising platforms for nanophotonic and plasmonic systems. Here, we report our analysis of single and dimer nanoantennas deposited on an aluminum-doped zinc oxide layer with an ENZ wavelength around 1.5 μm. Using near-field microscopy, far-field spectroscopy, finite-element numerical simulations, and a semi-analytic Fabry–Perot (FP) model, we show that single nanoantennas support highly dispersive plasmonic modes with less than unity effective mode index at wavelengths greater than the ENZ wavelength, which consequently fixes the resonance near the ENZ wavelength of the substrate. Furthermore, we observe a strong reduction in the near-field coupling between dimer nanoantennas via measurements of the resonance shift as a function of gap size. This reduction of near-field coupling allows one to design arrays of independently operating antennas with higher densities and thereby significantly improve the array characteristics, especially when targeting gradient metasurface implementations. Our results demonstrate the use of ENZ materials for increasing the versatility and functionality of plasmonic structures and provide foundational insight into this exotic material phenomenon.

https://doi.org/10.1364/OPTICA.5.001557

1. INTRODUCTION

Epsilon-near-zero (ENZ) materials shape and control light in extraordinary ways. Unlike conventional materials, the permittivity ε of an ENZ media is approximately zero, which for non-magnetic materials, implies a refractive index of zero ($n = \sqrt{\varepsilon}$). Consequently, an electromagnetic wave will have a nearly constant phase variation inside the ENZ media, alternatively interpreted as a "stretching" of the effective wavelength ($\lambda_{\text{eff}} = \lambda_0/n$) [1]. These static-like modes are the basis for many of the exotic phenomena and applications predicted theoretically and observed experimentally in ENZ materials, such as beam shaping and steering [2–4], subwavelength tunneling [5–7], and enhanced nonlinear interactions [8–13]. Even though there are some limitations for ENZ materials dictated by causality and Kramers–Kronig relations, the scope of applications for these unique materials keeps increasing [14]. For example, there is a growing interest to utilize the non-local ENZ fields for facilitating and observing non-classical coherence in systems of quantum emitters [15,16].

Although these examples highlight the remarkable properties of ENZ materials, it remains a substantial and open challenge to realize a system capable of supporting a vanishingly small permittivity. Current strategies include waveguides operating at cutoff [17], Dirac points in photonic crystals [18], engineered metamaterials [4,19,20], and naturally occurring polaritonic [21] and transparent conducting oxide (TCO) media [22,23]. The latter of these methods has many advantages over competing strategies, especially for obtaining ENZ at near-infrared wavelengths. TCOs are heavily doped, wide bandgap semiconductors that support free-carrier concentrations as large as 10^{21} cm^{-3} with corresponding cross-over frequencies throughout the near-infrared; furthermore, their interband absorption is confined to the ultraviolet due to their large bandgaps [23]. Therefore, loss near the cross-over frequency is small, and TCO films exhibit a permittivity that is naturally near zero without the need for advanced fabrication [24]. An additional advantage of ENZ TCO films is their tunability: the wide range of TCO materials and deposition techniques allow for ENZ wavelengths ranging from near- to mid-infrared wavelengths, and dynamic control—e.g., thermal annealing [25], optical excitation [8–10,26,27], electrical bias [28–31]—can shift the ENZ point by several hundred nanometers. Thus, TCO films are robust and flexible ENZ materials,

ideal for incorporating ENZ phenomena and applications into modern optoelectronic and photonic devices.

Recently, a growing body of research is investigating the effects of ENZ TCO films on plasmonic systems. Prior plasmon–ENZ work includes studies of single nanorods for resonance wavelength and radiation engineering [32,33], metamaterial split-ring resonators for polariton splitting [34,35], and plasmon-enhanced quantum wells for active terahertz control [36]. These studies demonstrate the great potential for plasmon–ENZ systems, but do not provide a thorough analysis or direct observation of the plasmon–ENZ coupling. Here, we investigate the plasmon–ENZ coupling in both single and dimer gold nanowire antennas with an aluminum-doped zinc oxide (Al:ZnO) TCO substrate exhibiting an ENZ permittivity at telecommunication wavelengths. We characterize the plasmonic response of single nanorods with far-field spectroscopy and directly observe the electric field maps of single nanorods at the ENZ wavelength using scattering near-field optical microscopy (SNOM). Numerical calculations using finite element simulations of the correspondent nanorod waveguide coupled with an analytic 1D FP model show excellent agreement with both far- and near-field measurements. We show that the plasmonic mode is highly dispersive and exhibits an effective mode index that is less than unity for wavelengths greater than the ENZ wavelength, resulting in the waveguide's wavelength being greater than the free-space excitation wavelength. Additionally, we demonstrate a strong suppression of near-field coupling between dimer nanorods on an ENZ substrate, which we attribute to the mode characteristics observed in single nanorod antennas.

2. RESULTS

A. Fabry–Perot Model for Single Nanorod

To explain and analyze both the near- and far-field response of nanorod antennas on ENZ substrates, we develop a FP model [37,38] of the plasmon modes upon normal plane-wave illumination (see Supplement 1). In this model, the nanorod is treated as a truncated waveguide, and incident light excites counter-propagating modes that reflect off either end of the nanorod's edges and form standing-wave interference. The interference is either constructive or destructive depending on parameters such as free-space wavelength or nanorod length. In this work we consider gold nanorods with a thickness of 40 nm and a width of 70 nm, deposited onto a 315-nm-thick layer of either Al:ZnO or ZnO on top of a glass substrate. The length of the nanorods varies from 100 to 2000 nm. It is obvious that the normal plane-wave illumination with electric field along the nanorod length will excite modes only from the short faces of the nanorod, as illustrated in Fig. 1(a). A modal analysis of the nanorod cross section using numerical simulations ensures only one supported quasi-bound mode. Permittivity values of gold were taken from the Palik handbook [39], while values of Al:ZnO and ZnO were extracted using spectroscopic ellipsometry from 315-nm-thick Al:ZnO and ZnO films deposited via pulsed laser deposition (PLD) onto glass slides (see Supplement 1). We found the ENZ wavelength of the Al:ZnO film to be 1475 nm with a concomitant dielectric permittivity of $\varepsilon_{ENZ} = 0 + i0.35$. The spectroscopic data was fitted using a Drude–Lorentz oscillator model to obtain permittivity values across the 400–2500 nm spectral range (Figs. S1 and S2 in Supplement 1). The

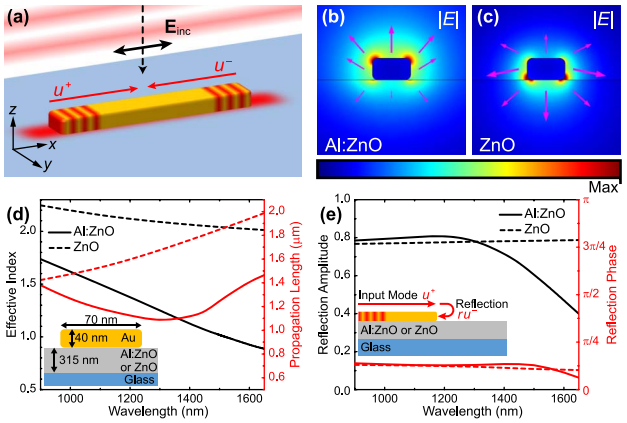

Fig. 1. Semi-analytical FP model for a single nanorod. (a) Sketch of a nanorod upon normal illumination, exciting two counter-propagating nanorod modes. (b), (c) Electric field distribution of nanorod waveguiding mode at the free-space wavelength of 1475 nm, deposited on (b) an Al:ZnO and (c) a ZnO substrate. Magenta arrows represent the transverse electric field. (d), (e) Numerically calculated effective mode index, propagation length, and reflection coefficient for a gold nanorod on the Al:ZnO (solid lines) and a ZnO substrate (dashed lines). Insets show the approximate configurations of the finite-element solver.

electric-field mode profiles for the free-space wavelength of 1475 nm are shown in Figs. 1(b) and 1(c). As reported previously, the mode field is concentrated in air for the ENZ substrate compared with the ZnO dielectric substrate [30]. The mode propagation properties are demonstrated in Fig. 1(d) in terms of the effective mode index N and propagation length L_{prop} for both Al:ZnO and ZnO substrates. We find that the effective mode index for the nanorod waveguide on the Al:ZnO has a strong negative dispersion and, furthermore, that it is less than unity for wavelengths past the ENZ wavelength of 1475 nm. On the contrary, the effective mode index for the nanorod waveguide on the ZnO is weakly dispersive with a value of approximately 2. Another simulation of the mode propagation in a terminated nanorod provides the complex reflection coefficient $r = |r| \exp[i\phi]$, where $|r|$ and ϕ are the amplitude and phase, respectively, of the reflection coefficient [Fig. 1(e)]. We find that both reflection amplitude and phase are nearly constant, both for Al:ZnO and ZnO substrates. The nanorod near field can then be calculated by summing the fields from all possible passes; consequently, the resonance condition is given by (see Supplement 1)

$$\frac{2\pi N}{\lambda_0} L + \phi = \pi + \pi m; \qquad m = 0, 2, 4, \ldots, \tag{1}$$

where L is the nanorod length, and λ_0 is the free-space wavelength. Physically, this implies that, at resonance condition, excitations from one end of the nanorod should constructively interfere with the out-of-phase excitation from the opposite end after accumulating a single propagation and reflection phase. We note that Eq. (1) describes bright modes only. The generalized FP model does not incorporate the excitation source and implies that, at resonance condition, the round trip should be in phase with initial excitation. Therefore, generalized FP models predict both bright (even m) and dark modes (odd m), the latter being inaccessible when using a normally incident plane wave source.

Equation (1) specifies the relation between nanorod length and resonance wavelength; consequently, the rate of change in resonance wavelength as a function of antenna length can be calculated:

$$\frac{d\lambda}{dL} = \frac{2\pi}{(\pi + \pi m - \phi)} \frac{N^2}{\left(N - \lambda_0 \frac{\partial N}{\partial \lambda}\right)}. \tag{2}$$

This result follows from our assumption that the reflection phase ϕ is wavelength independent, which is justified from our finite element method (FEM) analysis [Fig. 1(e)]. Equation (2) shows that for modes with largely dispersive effective index, the scaling law between resonant wavelength and antenna length is nonlinear. Furthermore, in the ideal limit $N \to 0$, the resonant wavelength becomes independent of antenna length, an effect referred to as a resonance pinning [32]. In contrast, for non-dispersive and non-zero effective mode index, the resonant wavelength should be simply proportional to the antenna length: $\lambda_0 = 2\pi NL/(\pi + \pi m - \phi)$.

In addition to the dispersive behavior of the resonance, we also use our model to accurately predict the near-field phase and magnitude of the single antennas. Figure 2 shows a side-by-side comparison of near-field maps obtained using full 3D FEM simulations (left column) and our semi-analytical FP model (right column) for a 600 nm antenna. The top and bottom rows show the maps obtained at different heights above the nanoantenna. As can be seen, there is a strong agreement between FP model and FEM simulations for E_y and E_z. A disagreement in E_x is caused by the presence of relatively strong exciting plane-wave and far-field antenna radiation in full 3D FEM simulations, while the FP model predicts only evanescent field distribution.

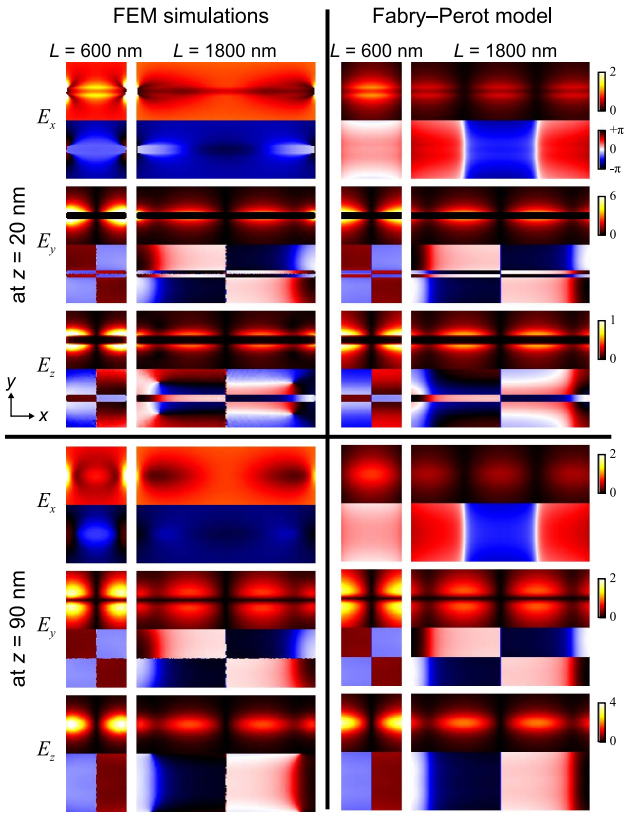

Fig. 2. Comparison of the field produced by full 3D FEM simulations and semi-analytical FP model. Simulations are done for gold antennas on Al:ZnO substrate at 1500 nm excitation from the bottom, polarized along the antenna length. The field was calculated at $z = 20$ nm (i.e., through the middle of the antenna, top) and $z = 90$ nm (i.e., 50 nm above the antenna, bottom) for two antenna lengths: 600 (left) and 1800 nm (right). The fields were normalized to the amplitude of the transmitted plane wave (note different color map scales).

B. Single Nanorod Far-Field Characterization

To verify the nonlinear scaling law and resonance pinning for antennas on an ENZ substrate, as followed from the above semi-analytic FP model, we fabricated and characterized nanorod antenna arrays on Al:ZnO substrate. Following the deposition of the Al:ZnO layer, we used standard electron-beam lithography, thermal metal evaporation, and lift-off methods to fabricate gold antenna arrays onto the Al:ZnO substrate. By setting the period along and perpendicular to the length of the antennas to $P_{\parallel} = 1200$ nm and $P_{\perp} = 600$ nm, respectively, we minimized antenna interaction while maintaining a significant antenna density. Each array consisted of antennas of lengths $L = 400$, 600, and 800 nm. Representative scanning electron microscope images are shown in Supplement 1, Fig. S3(a). We measured the far-field response of the single nanorod arrays using the cross-polarized reflection configuration of our spectroscopic ellipsometer, as shown in Fig. 3(a). Using this setup, we were able to collect the field radiated by the nanorod array while suppressing the strong reflected signal of the substrate. We fitted the reflection spectra with Lorentzian curves to extract the resonant wavelength. In Fig. 3(b) we plot the experimentally observed resonance wavelengths for antennas of lengths $L = 400$, 600, and 800 nm (crosses). In addition, we plot the resonant wavelengths predicted by using our FP model [Eq. (1)] (solid line), along with resonances for the scattering cross sections obtained using full-wave FEM simulations of isolated antennas (circles). For comparison, we included corresponding values for a ZnO substrate of similar thickness (red lines and dots). As can be seen, there is a good agreement between measurements and simulations, supporting the assumption of the negligible antenna interaction. Additionally, the resonance position predicted by our semi-analytical FP model is in good correspondence with results of full 3D simulations and measurements, even though the ellipsometer excitation angle in the experiment was slightly different than normal incidence. Finally, we verify that the resonance wavelength is largely nonlinear and becomes nearly independent of antenna length beyond the ENZ wavelength, an effect referred to as resonance pinning [32].

C. Single Nanorod Near-Field Characterization

To directly image the modes of the nanorods, we perform near-field characterization using SNOM. This technique allows us to simultaneously map both magnitude and phase of the near field, in addition to the sample topography (see Supplement 1). Because of the tip elongation along the z axis, the recorded near-field signal corresponds well to the normal z component of the electric field approximately 50 nm above the structure [40–42]. A schematic of our setup is shown in Fig. 4(a). We excite the sample from beneath using a 1475 nm laser, which was defocused in order to reproduce the plane-wave illumination. The sample contains a column of individual nanorods of lengths varied in 100 nm steps from 100 to 2000 nm; the spacing between antennas was 1000 nm. Figure 4(b) shows the topography and near-field maps

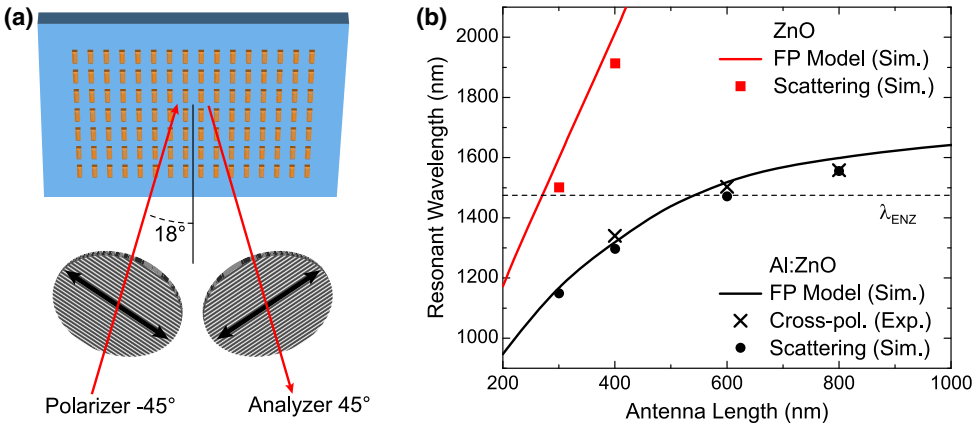

Fig. 3. Far-field characterization of nanorod arrays. (a) Cross-polarized configuration of our ellipsometer used for measuring the far-field scattering of the single antenna arrays. The input polarization is rotated −45° with respect to the nanorod's long axis and incident at 18°. The reflected light is passed through an analyzer set at the 45°. (b) Resonant wavelength as a function of antenna length for the Al:ZnO (black) and ZnO (red) substrates. The solid lines are calculated using the FP model, square and circular markers are results of scattering cross-section numerical calculations, and cross markers indicate experimental values obtained from cross-polarization spectroscopy. The dashed line indicates the ENZ wavelength of 1475 nm.

of the gold antennas on the underlying Al:ZnO substrate, along with the near-field magnitude and phase, calculated with full FEM simulations and predicted from our semi-analytic FP model as

$$E_z(x) \propto \sin\left(\frac{2\pi N}{\lambda_0}x + \frac{i}{L_{\text{prop}}}x\right). \tag{3}$$

We find the antennas of length less than 1000 nm support dipolar near-field distribution, as clearly seen by the phase profile; furthermore, we confirm the 600 nm antenna is at resonance with the 1475 nm excitation. The strong agreement between all near-field maps confirms the low effective mode index of the nanorod plasmonic mode for ENZ substrate. Additionally, the correspondence between near-field measurements and simulations verifies the optical properties of fabricated Al:ZnO substrate on the subwavelength scale, which makes it unique compared to the engineered ENZ metamaterials composed of stacked finite-size structures [4,18,19]. A similar comparison of recorded near-field maps with simulations for nanorods on ZnO substrate can be found in Supplement 1, Fig. S4.

D. Dimer Antenna Characterization

Having shown the ability for ENZ materials to significantly alter plasmonic resonances in single nanorods, we now turn our focus to dimer nanorods deposited on an ENZ substrate. In general, the resonance of a dimer pair will depend on the separation between rods due to the interparticle coupling [43,44]. For nanorod pairs oriented along their longitudinal axis, the resonant wavelength redshifts away from the isolated resonant wavelength as the separation decreases. To characterize the shift in resonance for dimer antennas on an ENZ substrate, we fabricated arrays of dimer nanorods, consisting of two $L = 400$ nm nanorods separated

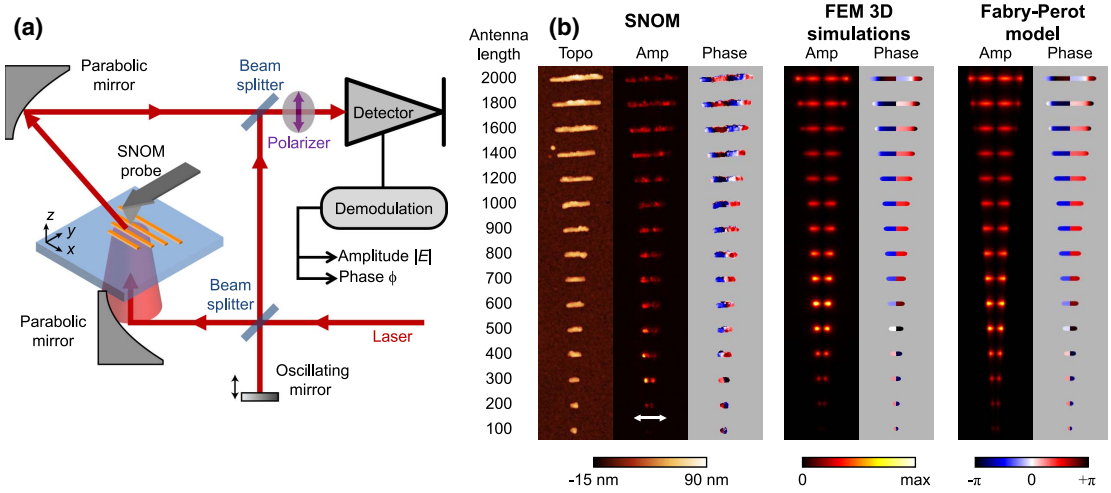

Fig. 4. Near-field optical microscopy of individual nanorods. (a) Schematic of the SNOM setup. (b) First column contains the measured topography, the magnitude, and the phase of the near field for gold antennas on Al:ZnO substrate at 1475 nm excitation, polarized along the antenna length (the polarization is shown with a white arrow). Second and third column are the corresponding z component of the electric field (E_z) calculated at 50 nm above nanorods with full 3D finite-element simulations and the semi-analytical FP model, respectively. Recorded topography and designed antenna parameters were used for masks in phase maps.

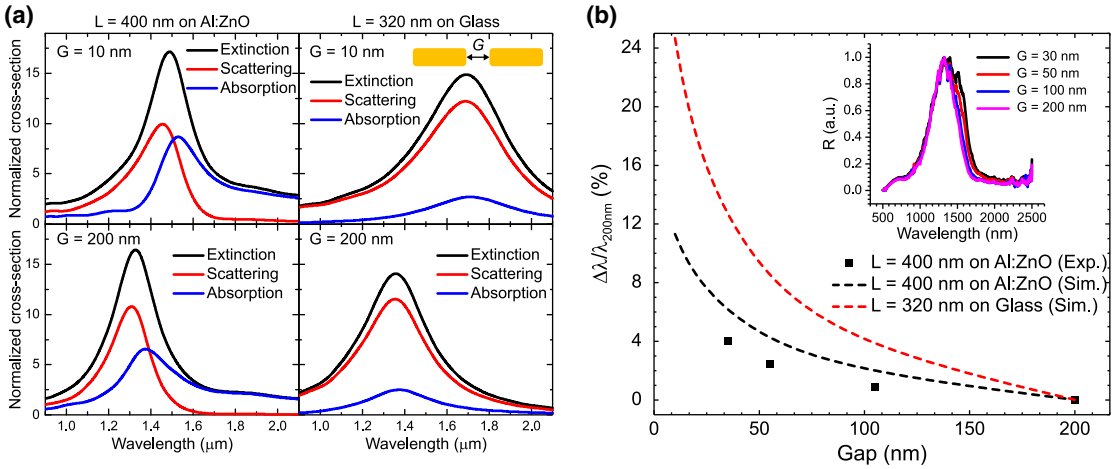

Fig. 5. Suppression of near-field coupling in dimer antennas. (a) Scattering, extinction, and absorption cross sections of dimer antennas on both Al:ZnO (left column) and glass (right column) substrates calculated with FEM. Gap distances of 10 and 200 nm are shown in the top and bottom rows, respectively. The antenna lengths are chosen such that the maximum cross sections coincide at a gap distance of 200 nm to clearly illustrate the distinction in total redshift. (b) Resonance wavelength redshift of dimer nanoantennas as a function of gap size, normalized to a gap of 200 nm. Black squares and line mark the experimentally measured and simulated, respectively, redshift of dimers on Al:ZnO as a function of gap size. Red line marks simulated redshift for dimers on glass. Inset shows the collected cross-polarized reflection spectra.

by a gap of 30, 50, 100, or 200 nm. We chose the period of all arrays to be $P_{\parallel} = 1300$ nm and $P_{\perp} = 500$ nm to maintain a constant and significant dimer density [see Supplement 1, Fig. S3(b)]. We employed FEM simulations to calculate the scattering, absorption, and extinction cross sections of gold dimer antennas on an Al:ZnO substrate; for comparison, we performed similar simulations for dimer nanorods on a glass substrate [Fig. 5(a)]. We chose the antenna length for dimers on glass to be 320 nm so that the resonance positions coincide for gap distances of 200 nm. Figures S5 and S6 of Supplement 1 contain numerically computed cross sections for dimers of varying gap sizes ($G = 10$, 20, 50, and 200 nm) and antenna lengths ($L = 300$, 400, 500, and 600 nm on Al:ZnO and $L = 320$ and 365 nm on glass), respectively; Fig. S7 is a compilation of both the absolute and relative redshifts in resonance as a function of gap size for all antenna lengths and substrates. For dimers on ENZ, we find the spectral redshift is reduced in comparison to antennas on glass and, furthermore, that the redshift decreases monotonically for increasing individual antenna length. Additionally, we find that the extinction cross section's spectral width is narrow as a result of the asymmetric scattering and absorption cross sections. In contrast, the redshift for dimer antennas on glass substrate is independent of antenna length, which agrees well with previous observations and analysis [43–45]. We measured the far-field scattering from our arrays of gold dimers using the same ellipsometry setup used to characterize arrays of single antennas. Figure 5(b) shows the experimentally obtained shift in resonance of $L = 400$ nm nanorod dimers (black squares), normalized to the resonant wavelength of dimers with $G = 200$ nm, as a function of gap size. Gap sizes were verified using scanning electron microscopy, and all resonant wavelengths were found by fitting the scattering spectrum with Lorentzian peaks [see inset of Fig. 5(b)]. Included in this figure are the shift in the resonance wavelength for $L = 400$ nm dimers on Al:ZnO (black line) and for $L = 320$ nm dimers on a glass substrate (red line). The antenna length of 320 nm for dimers on glass substrates was chosen such that the resonance shift occurred at the same spectral range as our ENZ wavelength. Our experimental results show a reduced redshift for antennas on the Al:ZnO substrate and corroborate our numerical simulations.

The reduced shift in resonance corresponds to a suppression of near-field coupling between the two nanoantennas of the dimer. In general, the normalized redshift of two plasmonic antennas as a function of gap size is proportional to the ratio of the interparticle near-field interaction to the single intraparticle Coulombic restoring force [44]. As we have shown from our single particle analysis and previous work [32], the near-field distribution of a single particle antenna is significantly altered at the ENZ regime of the substrate. In particular, we find that the field is primarily concentrated outside of the substrate past the ENZ wavelength since the air becomes the more optically dense media. The experimentally observed and numerically calculated strong reduction in the redshift, as compared to dimers on glass substrates, implies that the near-field interaction is thus suppressed. We do note that a reduction in the redshift will also follow from an increase in the individual antenna length of the dimer pair, because the intraparticle Coulombic restoring force goes as a $1/(\text{particle size})^3$ dependence and the normalized redshift, in the quasi-static dipole approximation, is given by $\Delta\lambda/\lambda_0 = (G/L + 1)^{-3}$, where G is the gap size and L is the antenna length [44]. Indeed, we do observe a slight decrease in redshift for antennas on a glass substrate for increasing antenna lengths (Supplement 1, Fig. S7). However, this contribution to the redshift reduction is small, even for large changes in antenna lengths, and cannot account fully for our observations. We thus conclude that the predominant mechanism is the suppression of near-field interactions due to the ENZ substrate. We note that the suppression of the near-field coupling is directly related to the ENZ nature of the substrate and is independent of the physical origin of the ENZ response; therefore, near-field suppression is a general feature of an ENZ substrate. Furthermore, we anticipate that an ENZ substrate will also result in similar suppression of near-field coupling between dimer antennas aligned along their transverse axis.

3. DISCUSSION

Maxwell's equations dictate that the fields in an ENZ material exhibit anomalous phase variation and the wavelength approaches infinity, i.e., $\lambda \to \infty$ as $\varepsilon \to 0$. This reasoning provides an intuitive picture for understanding and interpreting our results. As mentioned earlier, usually the scaling between the resonance wavelength and the physical length of the nanorod is approximately linear; however, as we have shown using Eq. (2), a nonlinear scaling occurs when the effective mode index is largely dispersive. Although the refractive index of the metal nanorod is itself dispersive, the electric fields of the plasmon mode are primarily located outside of the nanorod, and, accordingly, the mode's effective index is predominately determined by the surrounding material's index. This implies that the incident radiation's wavelength λ_0 and the nanorod's plasmon wavelength λ_{SPP} are proportional via $\lambda_{SPP} = \lambda_0/n_{eff}$, and that the nanorod's resonance wavelength changes linearly to an increase in antenna length for a non-dispersive dielectric environment. However, for an antenna located near an ENZ material, the plasmon modes of the nanorod will have a strong negative dispersion and exhibit a near-zero effective index, as we have observed [see Fig. 1(d)]. Consequentially, when the free-space wavelength of incident light is increased near the ENZ point, the effective mode index *decreases* and the plasmon wavelength will *increase* dependent on the magnitude of the dispersion; as such, the nanorod will resonate only at a longer length.

In summary, we have demonstrated dispersive, less than unity index plasmon modes with gold antennas on an Al:ZnO substrate with a near-infrared ENZ point. Furthermore, we demonstrated a reduced redshift in the resonance of dimer antennas on a ENZ substrate as a function of diminishing gap sizes because of suppressed near-field interactions. We have also developed a robust and accurate semi-analytic FP model for calculating electromagnetic near fields, dispersion, and resonances of single nanorod antennas on arbitrary substrates. Our observations and analysis open new directions for engineering the resonance of both single and coupled plasmonic antennas. For instance, the established reduction in near-field coupling allows one to design arrays of independently operating antennas with higher densities and thereby significantly improve the array characteristics, particularly when targeting gradient metasurface implementations. Moreover, by utilizing the suppressed near-field coupling, it may be possible to induce large modulation amplitudes by tuning the permittivity of the substrate around the ENZ point through either electrical or optical control. Additionally, it may be possible to utilize the near-zero index plasmon mode for increasing coherence between quantum emitters coupled to a plasmon system.

Funding. Air Force Office of Scientific Research (AFOSR) (FA9550-14-1-0389); H2020 European Research Council (ERC) (341054 (PLAQNAP)); U.S. Department of Energy (DOE) (DE-SC0017717).

Acknowledgment. This work is supported by the U.S. Department of Energy, Office of Basic Energy Sciences, Division of Materials Sciences and Engineering under Award DE-SC0017717 (sample fabrication, C.D. & K.C.), and Air Force Office of Scientific Research (AFOSR) award FA9550-14-1-0389 (far-field characterization, C.D.). V.A.Z., A.P., and S.I.B. acknowledge support from the European Research Council, Grant 341054 (PLAQNAP).

See Supplement 1 for supporting content.

†These authors contributed equally to this work.

REFERENCES

1. I. Liberal and N. Engheta, "Near-zero refractive index photonics," Nat. Photonics **11**, 149–158 (2017).
2. R. W. Ziolkowski, "Propagation in and scattering from a matched metamaterial having a zero index of refraction," Phys. Rev. E **70**, 046608 (2004).
3. A. Alù, M. G. Silveirinha, A. Salandrino, and N. Engheta, "Epsilon-near-zero metamaterials and electromagnetic sources: tailoring the radiation phase pattern," Phys. Rev. B **75**, 155410 (2007).
4. P. Moitra, Y. Yang, Z. Anderson, I. I. Kravchenko, D. P. Briggs, and J. Valentine, "Realization of an all-dielectric zero-index optical metamaterial," Nat. Photonics **7**, 791–795 (2013).
5. D. C. Adams, S. Inampudi, T. Ribaudo, D. Slocum, S. Vangala, N. A. Kuhta, W. D. Goodhue, V. A. Podolskiy, and D. Wasserman, "Funneling light through a subwavelength aperture with epsilon-near-zero materials," Phys. Rev. Lett. **107**, 133901 (2011).
6. R. Liu, Q. Cheng, T. Hand, J. J. Mock, T. J. Cui, S. A. Cummer, and D. R. Smith, "Experimental demonstration of electromagnetic tunneling through an epsilon-near-zero metamaterial at microwave frequencies," Phys. Rev. Lett. **100**, 023903 (2008).
7. M. G. Silveirinha and N. Engheta, "Theory of supercoupling, squeezing wave energy, and field confinement in narrow channels and tight bends using ε near-zero metamaterials," Phys. Rev. B **76**, 245109 (2007).
8. M. Z. Alam, I. De Leon, and R. W. Boyd, "Large optical nonlinearity of indium tin oxide in its epsilon-near-zero region," Science **352**, 795–797 (2016).
9. N. Kinsey, C. DeVault, J. Kim, M. Ferrera, V. M. Shalaev, and A. Boltasseva, "Epsilon-near-zero al-doped ZnO for ultrafast switching at telecom wavelengths," Optica **2**, 616–622 (2015).
10. L. Caspani, R. P. M. Kaipurath, M. Clerici, M. Ferrera, T. Roger, J. Kim, N. Kinsey, M. Pietrzyk, A. Di Falco, V. M. Shalaev, A. Boltasseva, and D. Faccio, "Enhanced nonlinear refractive index in ε-near-zero materials," Phys. Rev. Lett. **116**, 233901 (2016).
11. H. Suchowski, K. O'Brien, Z. J. Wong, A. Salandrino, X. Yin, and X. Zhang, "Phase mismatch-free nonlinear propagation in optical zero-index materials," Science **342**, 1223–1226 (2013).
12. B. T. Diroll, P. Guo, R. P. H. Chang, and R. D. Schaller, "Large transient optical modulation of epsilon-near-zero colloidal nanocrystals," ACS Nano **10**, 10099–10105 (2016).
13. T. S. Luk, D. de Ceglia, S. Liu, G. A. Keeler, R. P. Prasankumar, M. A. Vincenti, M. Scalora, M. B. Sinclair, and S. Campione, "Enhanced third harmonic generation from the epsilon-near-zero modes of ultrathin films," Appl. Phys. Lett. **106**, 151103 (2015).
14. M. H. Javani and M. I. Stockman, "Real and imaginary properties of epsilon-near-zero materials," Phys. Rev. Lett. **117**, 107404 (2016).
15. E. Shahmoon and G. Kurizki, "Nonradiative interaction and entanglement between distant atoms," Phys. Rev. A **87**, 033831 (2013).
16. R. Fleury and A. Alù, "Enhanced superradiance in epsilon-near-zero plasmonic channels," Phys. Rev. B **87**, 201101 (2013).
17. E. J. R. Vesseur, T. Coenen, H. Caglayan, N. Engheta, and A. Polman, "Experimental verification of n = 0 structures for visible light," Phys. Rev. Lett. **110**, 013902 (2013).
18. X. Huang, Y. Lai, Z. H. Hang, H. Zheng, and C. T. Chan, "Dirac cones induced by accidental degeneracy in photonic crystals and zero-refractive-index materials," Nat. Mater. **10**, 582–586 (2011).
19. Y. Li, S. Kita, P. Muñoz, O. Reshef, D. I. Vulis, M. Yin, M. Lončar, and E. Mazur, "On-chip zero-index metamaterials," Nat. Photonics **9**, 738–742 (2015).
20. R. Maas, J. Parsons, N. Engheta, and A. Polman, "Experimental realization of an epsilon-near-zero metamaterial at visible wavelengths," Nat. Photonics **7**, 907–912 (2013).
21. J. D. Caldwell, L. Lindsay, V. Giannini, I. Vurgaftman, T. L. Reinecke, S. A. Maier, and O. J. Glembocki, "Low-loss, infrared and terahertz

nanophotonics using surface phonon polaritons," Nanophotonics **4**, 44–68 (2015).
22. G. V. Naik, J. Kim, and A. Boltasseva, "Oxides and nitrides as alternative plasmonic materials in the optical range," Opt. Mater. Express **1**, 1090–1099 (2011).
23. G. V. Naik, V. M. Shalaev, and A. Boltasseva, "Alternative plasmonic materials: beyond gold and silver," Adv. Mater. **25**, 3264–3294 (2013).
24. J. Kim, G. V. Naik, A. V. Gavrilenko, K. Dondapati, V. I. Gavrilenko, S. M. Prokes, O. J. Glembocki, V. M. Shalaev, and A. Boltasseva, "Optical properties of gallium-doped zinc oxide-a low-loss plasmonic material: first-principles theory and experiment," Phys. Rev. X **3**, 041037 (2013).
25. J. Kim, S. Choudhury, C. DeVault, Y. Zhao, A. V. Kildishev, V. M. Shalaev, A. Alù, and A. Boltasseva, "Controlling the polarization state of light with plasmonic metal oxide metasurface," ACS Nano **10**, 9326–9333 (2016).
26. T. Tyborski, S. Kalusniak, S. Sadofev, F. Henneberger, M. Woerner, and T. Elsaesser, "Ultrafast nonlinear response of bulk plasmons in highly doped ZnO layers," Phys. Rev. Lett. **115**, 147401 (2015).
27. M. Clerici, N. Kinsey, C. DeVault, J. Kim, E. G. Carnemolla, L. Caspani, A. Shaltout, D. Faccio, V. Shalaev, A. Boltasseva, and M. Ferrera, "Controlling hybrid nonlinearities in transparent conducting oxides via two-colour excitation," Nat. Commun. **8**, 15829 (2017).
28. J. Park, J.-H. Kang, S. J. Kim, X. Liu, and M. L. Brongersma, "Dynamic reflection phase and polarization control in metasurfaces," Nano Lett. **17**, 407–413 (2017).
29. H. W. Lee, G. Papadakis, S. P. Burgos, K. Chander, A. Kriesch, R. Pala, U. Peschel, and H. A. Atwater, "Nanoscale conducting oxide plasmostor," Nano Lett. **14**, 6463–6468 (2014).
30. Y.-W. Huang, H. W. H. Lee, R. Sokhoyan, R. A. Pala, K. Thyagarajan, S. Han, D. P. Tsai, and H. A. Atwater, "Gate-tunable conducting oxide metasurfaces," Nano Lett. **16**, 5319–5325 (2016).
31. X. Liu, J.-H. Kang, H. Yuan, J. Park, S. J. Kim, Y. Cui, H. Y. Hwang, and M. L. Brongersma, "Electrical tuning of a quantum plasmonic resonance," Nat. Nanotechnol. **12**, 866–870 (2017).
32. J. Kim, A. Dutta, G. V. Naik, A. J. Giles, F. J. Bezares, C. T. Ellis, J. G. Tischler, A. M. Mahmoud, H. Caglayan, O. J. Glembocki, A. V. Kildishev, J. D. Caldwell, A. Boltasseva, and N. Engheta, "Role of epsilon-near-zero substrates in the optical response of plasmonic antennas," Optica **3**, 339–346 (2016).
33. S. A. Schulz, A. A. Tahir, M. Z. Alam, J. Upham, I. De Leon, and R. W. Boyd, "Optical response of dipole antennas on an epsilon-near-zero substrate," Phys. Rev. A **93**, 063846 (2016).
34. S. Campione, J. R. Wendt, G. A. Keeler, and T. S. Luk, "Near-infrared strong coupling between metamaterials and epsilon-near-zero modes in degenerately doped semiconductor nanolayers," ACS Photon. **3**, 293–297 (2016).
35. S. Campione, S. Liu, A. Benz, J. F. Klem, M. B. Sinclair, and I. Brener, "Epsilon-near-zero modes for tailored light-matter interaction," Phys. Rev. Appl. **4**, 044011 (2015).
36. S. Vassant, A. Archambault, F. Marquier, F. Pardo, U. Gennser, A. Cavanna, J. L. Pelouard, and J. J. Greffet, "Epsilon-near-zero mode for active optoelectronic devices," Phys. Rev. Lett. **109**, 237401 (2012).
37. E. Cubukcu and F. Capasso, "Optical nanorod antennas as dispersive one-dimensional Fabry-Pérot resonators for surface plasmons," Appl. Phys. Lett. **95**, 201101 (2009).
38. J. Dorfmüller, R. Vogelgesang, R. T. Weitz, C. Rockstuhl, C. Etrich, T. Pertsch, F. Lederer, and K. Kern, "Fabry-Pérot resonances in one-dimensional plasmonic nanostructures," Nano Lett. **9**, 2372–2377 (2009).
39. E. D. Palik, ed., *Handbook of Optical Constants of Solids* (Academic, 1985).
40. A. Andryieuski, V. A. Zenin, R. Malureanu, V. S. Volkov, S. I. Bozhevolnyi, and A. V. Lavrinenko, "Direct characterization of plasmonic slot waveguides and nanocouplers," Nano Lett. **14**, 3925–3929 (2014).
41. V. A. Zenin, A. Andryieuski, R. Malureanu, I. P. Radko, V. S. Volkov, D. K. Gramotnev, A. V. Lavrinenko, and S. I. Bozhevolnyi, "Boosting local field enhancement by on-chip nanofocusing and impedance-matched plasmonic antennas," Nano Lett. **15**, 8148–8154 (2015).
42. V. A. Zenin, S. Choudhury, S. Saha, V. M. Shalaev, A. Boltasseva, and S. I. Bozhevolnyi, "Hybrid plasmonic waveguides formed by metal coating of dielectric ridges," Opt. Express **25**, 12295–12302 (2017).
43. P. K. Jain, W. Huang, and M. A. El-Sayed, "On the universal scaling behavior of the distance decay of plasmon coupling in metal nanoparticle pairs: a plasmon ruler equation," Nano Lett. **7**, 2080–2088 (2007).
44. P. K. Jain and M. A. El-Sayed, "Surface plasmon coupling and its universal size scaling in metal nanostructures of complex geometry: elongated particle pairs and nanosphere trimers," J. Phys. Chem. C **112**, 4954–4960 (2008).
45. J. Aizpurua, G. W. Bryant, L. J. Richter, F. J. García de Abajo, B. K. Kelley, and T. Mallouk, "Optical properties of coupled metallic nanorods for field-enhanced spectroscopy," Phys. Rev. B **71**, 235420 (2005).